Uncompensated Polarization in Incommensurate Modulations of Perovskite Antiferroelectrics

Tao Ma,[1,‡] Zhongming Fan,[2,‡] Bin Xu,[3,4] Tae-Hoon Kim,[1] Ping Lu,[5] Laurent Bellaiche,[3] Matthew J. Kramer,[1,2] Xiaoli Tan,[2,*] and Lin Zhou[1,2,†]

[1]*Ames Laboratory, U.S. Department of Energy, Ames, Iowa 50011, USA*
[2]*Department of Materials Science and Engineering, Iowa State University, Ames, Iowa 50011, USA*
[3]*Physics Department and Institute for Nanoscience and Engineering, University of Arkansas, Fayetteville, Arkansas 72701, USA*
[4]*School of Physical Science and Technology, Soochow University, Suzhou, Jiangsu 215006, China*
[5]*Sandia National Laboratories, P.O. Box 5800, MS 1411, Albuquerque, New Mexico 87185, USA*

(Received 24 May 2019; published 19 November 2019)

Complex polar structures of incommensurate modulations (ICMs) are revealed in chemically modified $PbZrO_3$ perovskite antiferroelectrics using advanced transmission electron microscopy techniques. The Pb-cation displacements, previously assumed to arrange in a fully compensated antiparallel fashion, are found to be either antiparallel, but with different magnitudes, or in a nearly orthogonal arrangement in adjacent stripes in the ICMs. *Ab initio* calculations corroborate the low-energy state of these arrangements. Our discovery corrects the atomic understanding of ICMs in $PbZrO_3$-based perovskite antiferroelectrics.

DOI: 10.1103/PhysRevLett.123.217602

Antiferroelectric (AFE) crystals possess dipoles within unit cells in an antiparallel arrangement so that the macroscopic polarization is fully compensated [1]. Under the application of an electric field above the critical value, E_F, the antiparallel dipoles can be forced to align parallel, leading to the transition to a ferroelectric (FE) phase [2]. And presumably, they resume the antiparallel arrangements upon removal of the applied field [3–5]. Consequently, double hysteresis loops with nearly zero remanent polarizations are recorded from the polarization vs electric-field (P-E) measurement [4,6]. The most widely studied AFEs are based on $PbZrO_3$, which crystallizes in a distorted perovskite structure with antiparallel Pb-cation displacements. Such a structure is equivalent to a perovskite with commensurate modulations (CMs) of $\frac{1}{4}\{110\}_c$, i.e., a wavelength of four layers of its pseudocubic $\{110\}_c$ plane [7–10]. As shown in Fig. 1(a), the antiparallel arrangement of the Pb-cation displacements in $PbZrO_3$ is directly verified by the mapping of Pb-displacement vectors on a high-angle annular dark-field scanning transmission electron microscopy (HAADF-STEM) image. A schematic diagram [7] illustrating the antiparallel arrangement in adjacent stripes is redrawn in Fig. 1(b).

Because E_F in $PbZrO_3$ at room temperature exceeds its dielectric strength [12], Sn and Ti in conjunction with a small amount of Nb or La are added to reduce E_F for practical applications [13–18]. The reduction in E_F is accompanied by the formation of $\frac{1}{n}\{110\}_c$ (n is a non-integer, typically between 6 and 8) incommensurate modulations (ICMs), which manifest themselves as fine fringes in diffraction-contrast TEM images and satellite spots in reciprocal space [Fig. 1(c)] [13,16–18]. However, the dipole arrangement in these incommensurate phases remains elusive, due largely to their complex subdomain microstructure [16,17]. Earlier studies interpreted the ICMs as an ensemble of commensurate phases with coexisting different integer n values (e.g., $n = 6$, 7, or 8) [11,18,19]. The dipoles in adjacent stripes were believed to keep a constant magnitude in an antiparallel arrangement across neighboring stripes so that the overall polarization in AFE domains remain fully compensated [Fig. 1(d)] [11].

Here we demonstrate that the classic view of the dipole arrangement in ICMs is incorrect. With direct cation displacement mapping in a series of $PbZrO_3$-based compositions ($Pb_{0.99}Nb_{0.02}[(Zr_{0.57}Sn_{0.43})_{1-y}Ti_y]_{0.98}O_3$, referred to as PZ-100$y$ hereafter), we reveal that the Pb displacements in adjacent stripes of ICMs are not fully compensated most of the time. Instead, they are either antiparallel, but with different magnitudes along opposing directions, or in a nearly orthogonal arrangement; i.e., these previously thought fully compensated AFE domains, in fact, bear a net polarization. These polar AFE domains transition into the FE phase under applied electric fields and resume their original configuration upon removal of the field, leading to the AFE-like double P-E hysteresis loops (see Fig. S1 in the Supplemental Material [20]).

Figure 2 illustrates the representative TEM micrographs of chemically modified $PbZrO_3$ ceramics. Bright-field TEM images in Figs. 2(a), 2(d), and 2(g) (top row) from PZ-3, PZ-5, and PZ-6, respectively, show typical 90° AFE domains with textured contrast. Selected area electron diffraction (SAED) patterns along the $[001]_c$ zone axis

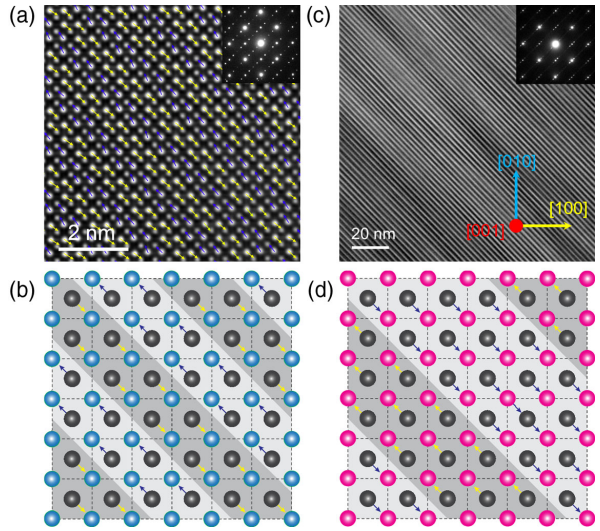

FIG. 1. (a) Typical HAADF-STEM image of CMs in $PbZrO_3$, with the SAED pattern shown in the inset. A Pb-displacement vector map is overlaid on the image, showing the antiparallel displacements of Pb cations in adjacent stripes. (b) Schematic model of the CMs for $PbZrO_3$ proposed by Sawaguchi *et al.* [7]. *A* site (Pb), gray; *B* site (Zr), blue. (c) Typical bright-field TEM image of ICMs in a Sn, Ti, Nb comodified $PbZrO_3$ ceramic, with the SAED pattern shown in the inset. The ICMs are rendered as fine fringes with a periodicity of ~2 nm. (d) Schematic model of the ICMs as a mixture of stripes with a stochastic thickness of two to four layers of the $\{110\}_c$ plane, proposed by He and Tan [11]. *A* site (Pb), gray; *B* site (Zr, Sn, Ti, Nb), pink.

(shown in the insets) taken from the domain boundary region present the satellite spots, $ha^* + kb^* + lc^* \pm 1/n(a^* + b^*)$ (h, k, l are integers, and n represents the periodicity of ICMs indicated in SAED), which are resulted from the ICMs inside each domain [5]. Atomic-resolution HAADF-STEM images were recorded from the upper and the lower domains of each sample, shown in the second and third rows, respectively. The atomic positions of both the *A*-site (Pb) and *B*-site (Zr, Sn, Ti, and Nb) columns were determined by fitting the intensity maxima in these images using a two-dimensional Gaussian function (see the Supplemental Material [20] for details). The off-center displacements of Pb cations were calculated with respect to the geometric center of the four surrounding *B*-site columns and overlaid on the HAADF images. Strikingly, we found that the dipole arrangement in ICMs deviates from the "fully-compensated antiparallel model" depicted in Fig. 1(d). In the upper domains, despite the Pb-displacement vectors being basically antiparallel in adjacent stripes, those in the wider stripes (blue) have larger magnitudes than the ones in the narrower stripes (yellow), as shown in Figs. 2(b), 2(e), and 2(h). This imbalance in the magnitudes becomes more obvious from PZ-3 [Fig. 2(b)] to PZ-6 [Fig. 2(h)] when Ti content gets higher. In the lower domains, Figs. 2(c), 2(f), and 2(i), the Pb displacements tend to rotate from the two antiparallel $\langle 110\rangle_c$ toward the two orthogonal $\langle 100\rangle_c$ directions. Such rotation becomes more apparent when Ti content increases. In PZ-3, the rotation is mainly noticed in the narrower stripes [yellow in Fig. 2(c)], whereas in PZ-5 almost all of the Pb-displacement vectors in the narrower stripes [yellow in Fig. 2(f)] and a large portion of those in the wider stripes [blue in Fig. 2(f)] turned to the $\langle 100\rangle_c$ directions. In PZ-6, the Pb displacements are almost along either $[100]_c$ or $[0\bar{1}0]_c$ [Fig. 2(i)], forming an orthogonal arrangement of dipoles in adjacent stripes.

We conducted HAADF-STEM image simulations under our experimental conditions. The results confirmed that the observed Pb displacements reflect the real atomic configuration of dipoles rather than artifacts from the optical system, sample thickness, and/or crystal tilts [28,29] (see Table S1 and Fig. S2 in the Supplemental Material [20]). Moreover, HAADF-STEM imaging and atomic-scale energy-dispersive x-ray spectroscopy (EDS) mapping show uniform chemistry across the domain boundaries as well as within the neighboring stripes (see Fig. S3 in the Supplemental Material [20]), indicating that the observed dipole arrangement is not directly associated with the local element distribution. Since the atomic structures found in the composition series are distinct from both the classic AFE and FE models, we denote these 90° domains as "transitional state" and differentiate the two across the boundary as the "antiparallel" side, Figs. 2(b), 2(e), and 2(h), and the "orthogonal" side, Figs. 2(c), 2(f), and 2(i).

To better compare the Pb displacements in the series with different Ti content, we extract the magnitudes of Pb displacements from the vector maps in Fig. 2 by averaging ten atomic layers of Pb along the stripes. The corresponding polarization due to Pb displacements are quantified through the equation

$$P = \frac{e}{V}\sum_{i=1}^{N} Z^* \delta_i,$$

where N is the number of Pb atoms in the box under consideration, V is the volume of the box, δ_i is the displacement of the ith Pb, and Z^* is the Born effective charge for Pb, given as 3.92 in cubic $PbZrO_3$ by Zhong *et al.* [30]. These data are plotted against the Pb positions in Figs. 3(a)–3(c). It can be seen that the polarization due to Pb displacements fluctuates across the modulations, rendering wavelike curves. This sinusoidal fashion of the Pb displacements across the ICMs was previously reported by MacLaren *et al.* [31]. However, on the antiparallel side, these polarization curves (blue) shift toward one side of the two $\langle 110\rangle_c$, corresponding to the imbalanced Pb displacements in opposing directions. In addition, the shift gets more severe as Ti content increases in the composition series. Accompanying with the shift on the antiparallel side is a slight increase in polarization components along $\langle 100\rangle_c$ on the orthogonal side (pink).

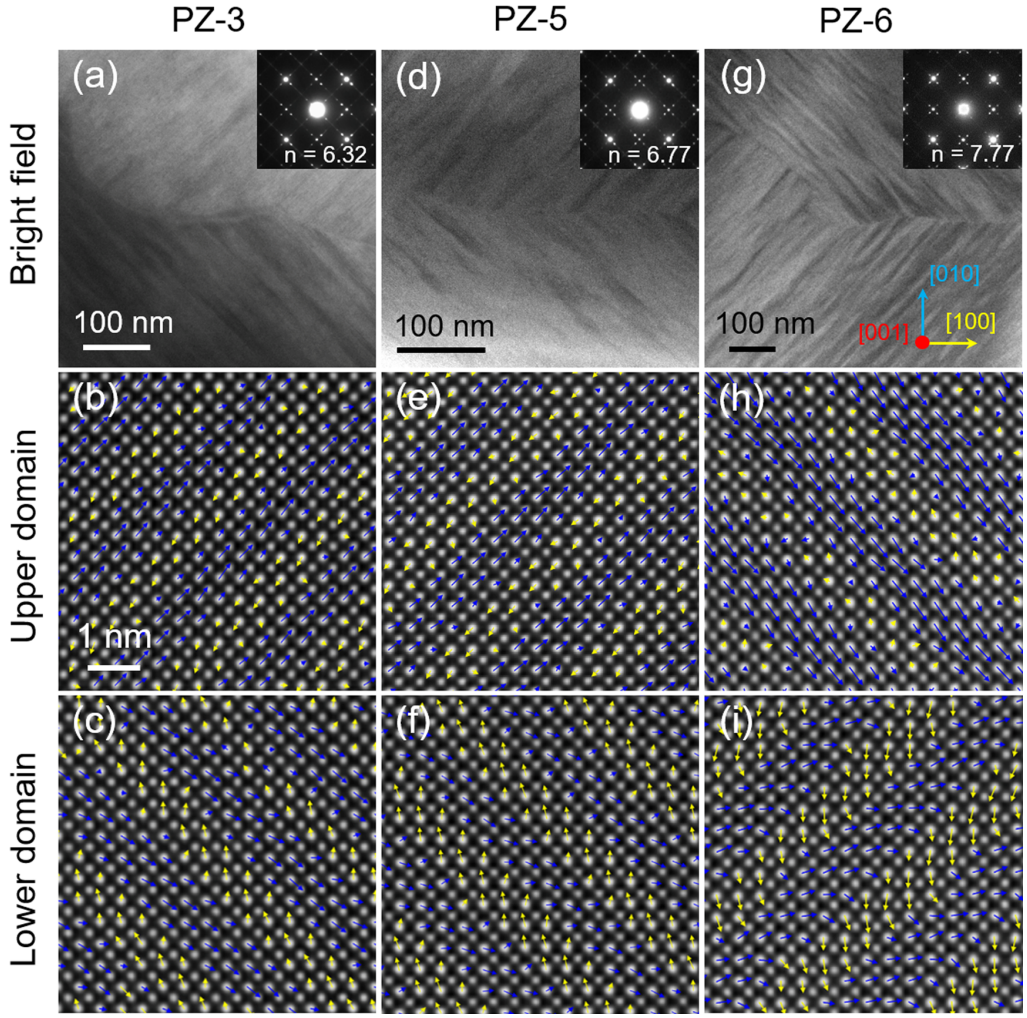

FIG. 2. The top row is the typical bright-field TEM images of 90° domains in (a) PZ-3, (d) PZ-5, and (g) PZ-6. (Insets) SAED patterns taken from the domain boundary region showing two sets of satellite spots, from which the periodicity of the ICMs (n value) was calculated. The middle row shows the Pb-displacement vector maps overlaid on the HAADF-STEM images taken from the upper domains in (b) PZ-3, (e) PZ-5, and (h) PZ-6. The Pb displacements in this row are in an antiparallel arrangement, but those in the wider stripes (blue) have a larger magnitude than the ones in the narrower stripes (yellow). The bottom row presents the Pb-displacement vector maps taken from the lower domains in (c) PZ-3, (f) PZ-5, and (i) PZ-6, where the Pb displacements tend to form in a nearly orthogonal arrangement in adjacent stripes.

Such unique dipole arrangements in the ICMs lead to uncompensated polarization within these transitional-state domains. The magnitude of the net polarization is estimated by summing the polarization vectors from corresponding vector maps and displayed in Fig. 3(d). The calculated net polarization increases with Ti content in the series, e.g., 5.89 and 5.46 $\mu C/cm^2$ for the antiparallel and the orthogonal side, respectively, in PZ-3, and 11.48 and 11.07 $\mu C/cm^2$ for the antiparallel and the orthogonal side, respectively, in PZ-6. This tendency toward increasing net polarization in transitional-state domains, together with the reduced E_F (see Fig. S1 in the Supplemental Material [20]) in the composition series, confirms that Ti on B sites in perovskite oxides promotes FE ordering. Furthermore, the presence of uncompensated polarization may be the reason for the fact that all 90° boundaries analyzed in this Letter have the antiparallel arrangement on one side, and the orthogonal arrangement on the other side. A 90° boundary with the same dipole arrangement on both sides would carry a very high depolarization energy.

More insight on the formation of the antiparallel and orthogonal domains was gained from density functional theory (DFT) calculations (at 0 K). To assess the stability of these polar domain structures, they were studied for both $PbZrO_3$ and $Pb(Zr_{0.5}Sn_{0.5})O_3$ and compared with the AFE phase (*Pbam*-like), the ground state of $PbZrO_3$. Note that $Pb(Zr_{0.5}Sn_{0.5})O_3$ is considered to largely resemble the experimental compositions at a feasible computational cost. The DFT optimized antiparallel and orthogonal domain structures for $PbZrO_3$ and $Pb(Zr_{0.5}Sn_{0.5})O_3$ are

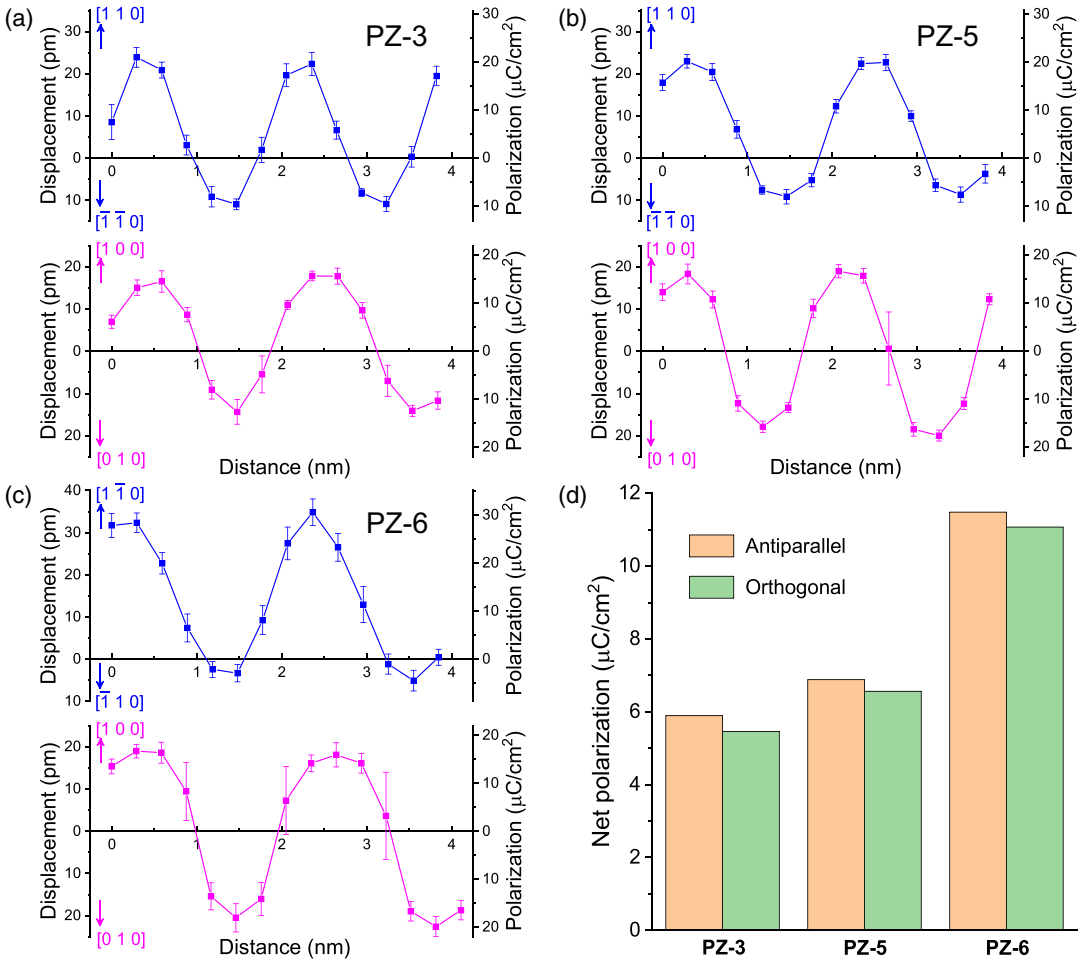

FIG. 3. (a)–(c) Pb-displacement magnitudes, extracted from the Pb-displacement vector maps, and the corresponding polarizations in (a) PZ-3, (b) PZ-5, and (c) PZ-6. The upper plots in each panel (blue) are from the antiparallel side showing the components along the two antiparallel $\langle 110\rangle_c$ directions, whereas the lower plots in each panel (pink) are from the orthogonal sides showing the components along the two orthogonal $\langle 100\rangle_c$ directions. The displacements were averaged from ten layers of Pb cations along the length direction of the ICM stripes. (d) Overall polarizations in the antiparallel and orthogonal sides of the three specimens calculated from the corresponding vector maps.

displayed in Figs. 4(b)–4(e), and their ground state structures (*Pbam*-like) are present in Figs. S4(a) and S4(b) in the Supplemental Material [20]. Note that the Pb displacements obtained by DFT are mostly in the $(001)_c$ plane with zero or negligible out-of-plane components (see the detailed atom position and displacement data in Tables S2–S7 in the Supplemental Material [20]). For the relaxed transitional-state domain structures in pure $PbZrO_3$ as shown in Figs. 4(b) and 4(c), they retain the characteristics of the antiparallel and orthogonal domains found in the HAADF-STEM images, and their energies are only slightly higher than in the AFE phase [Fig. 4(a)]. The antiparallel structure has an energy of 4.3 meV/f.u. higher than in the AFE phase, and it is 6.8 meV/f.u. for the orthogonal structure. Similarly, the antiparallel and orthogonal structures are also stable in $Pb(Zr_{0.5}Sn_{0.5})O_3$, as shown in Figs. 4(d) and 4(e), and compared with $PbZrO_3$, the relative energies are only 2.8 and 6.7 meV/f.u. higher than in the AFE phase. A close examination of the orthogonal structure reveals that the Pb displacements in the "blue" and "yellow" stripes in $Pb(Zr_{0.5}Sn_{0.5})O_3$ are aligned closer to the $[100]_c$ and $[010]_c$ directions, respectively, than in $PbZrO_3$. The optimized structures and the small energy differences indicate that the antiparallel and orthogonal domain structures are metastable, and the stability improves with the substitution of Sn on the *B* sites. Note that the transitional-state domain structures are more complex than the AFE phase; therefore, they are likely to be more favorable at finite temperature due to the entropy contribution to the free energy. Furthermore, the stabilization of the transitional-state domain structures is related to the existence of a bilinear coupling between the Pb displacements and the oxygen octahedral tilting [32,33], such that the octahedra develop an accommodating pattern to lower the energy cost of forming Pb modulations (details are discussed in the Supplemental Material [20]).

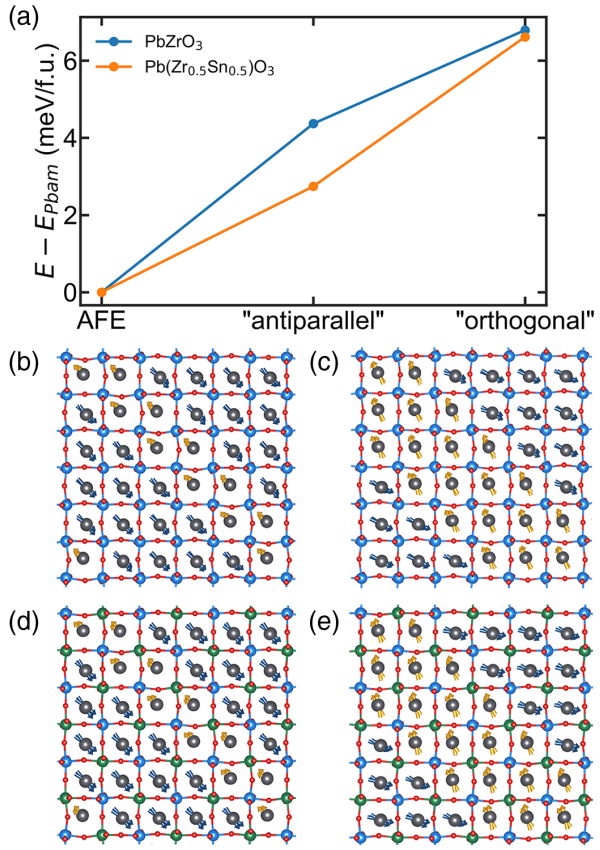

FIG. 4. (a) DFT calculated energies of the antiparallel and orthogonal domain structures relative to the AFE phase (*Pbam*-like) for $PbZrO_3$ and $Pb(Zr_{0.5}Sn_{0.5})O_3$. (b),(c) DFT optimized antiparallel and orthogonal domain structures of $PbZrO_3$. (d), (e) DFT optimized antiparallel and orthogonal domain structures of $Pb(Zr_{0.5}Sn_{0.5})O_3$. Pb, gray; Zr, blue; Sn, green; O, red. Pb displacements are denoted in blue and yellow in different stripes. The atom position and displacement data used to create (b)–(e) are listed in Tables S4, S5, S6, and S7, respectively, in the Supplemental Material [20].

The presence of net polarization in the transitional-state domains appears to contradict the measurement of double *P-E* hysteresis loops on bulk samples in this composition series (Fig. S1 in the Supplemental Material [20]). To reconcile this conflict, we performed *in situ* electric-biasing TEM experiments. The results show the transition of a transitional-state domain to the FE phase under an applied electric field, and its resumption to the original transitional-state domain structure upon the removal of the field (see Fig. S5 in the Supplemental Material [20] for details). The full recovery of the hierarchical structure (domains, boundary, ICMs, and cation displacements) hence explains the nearly zero remnant polarization measured on bulk samples.

In summary, we uncover at the atomic scale that the Pb displacements in ICMs of $PbZrO_3$-based AFEs are either antiparallel but imbalanced or in a nearly orthogonal arrangement. The uncompensated dipole moments introduce nonzero net polarizations in 90° AFE domains, and their magnitudes increase with Ti content. In contrast to the polar nature of the microstructure, macroscopically these ceramics behave in an AFE manner with the characteristic *P-E* double hysteresis loops of negligible remnant polarization. Such unique structures in incommensurate modulated $PbZrO_3$-based AFEs can be viewed as a transitional state between long-range FE and AFE orderings. Experiments on other inorganic AFE oxides may also find such a transitional state in the future.

This work was supported in part by the National Science Foundation (NSF) through Grant No. DMR-1700014. All electron microscopy work was performed at the Sensitive Instrument Facility at Ames Laboratory, which is operated for the U.S. Department of Energy (DOE) by Iowa State University under Contract No. DE-AC02-07CH11358. B. X. and L. B. thank ONR Grant No. N00014-17-1-2818 and DARPA Grant No. HR0011-15-2-0038 under the MATRIX program.

*Corresponding author.
xtan@iastate.edu
†Corresponding author.
linzhou@ameslab.gov
‡T. M. and Z. F. contributed equally to this work.

[1] C. Kittel, Phys. Rev. **82**, 729 (1951).
[2] G. Shirane, E. Sawaguchi, and Y. Takagi, Phys. Rev. **84**, 476 (1951).
[3] X. Tan, J. Frederick, C. Ma, W. Jo, and J. Rödel, Phys. Rev. Lett. **105**, 255702 (2010).
[4] S.-E. Park, M.-J. Pan, K. Markowski, S. Yoshikawa, and L. E. Cross, J. Appl. Phys. **82**, 1798 (1997).
[5] X. Tan, C. Ma, J. Frederick, S. Beckman, and K. G. Webber, J. Am. Ceram. Soc. **94**, 4091 (2011).
[6] B. K. Mani, C.-M. Chang, S. Lisenkov, and I. Ponomareva, Phys. Rev. Lett. **115**, 097601 (2015).
[7] E. Sawaguchi, H. Maniwa, and S. Hoshino, Phys. Rev. **83**, 1078 (1951).
[8] K. Yamasaki, Y. Soejima, and K. F. Fischer, Acta Crystallogr. Sect. B **54**, 524 (1998).
[9] F. Jona, G. Shirane, and R. Pepinsky, Phys. Rev. **105**, 849 (1957).
[10] D. L. Corker, A. M. Glazer, J. Dec, K. Roleder, and R. W. Whatmore, Acta Crystallogr. Sect. B **53**, 135 (1997).
[11] H. He and X. Tan, Phys. Rev. B **72**, 024102 (2005).
[12] O. E. Fesenko, R. V. Kolsesova, and Y. G. Sindeyev, Ferroelectrics **20**, 177 (1978).
[13] Y.-J. Chang, J.-Y. Lian, and Y.-l. Wang, Appl. Phys. A **36**, 221 (1985).
[14] D. Berlincourt, IEEE Trans. Sonics Ultrason. **13**, 116 (1966).
[15] W. Pan, Q. Zhang, A. Bhalla, and L. E. Cross, J. Am. Ceram. Soc. **72**, 571 (1989).
[16] D. Viehland, D. Forst, Z. Xu, and J.-F. Li, J. Am. Ceram. Soc. **78**, 2101 (1995).
[17] D. Viehland, X. H. Dai, J. F. Li, and Z. Xu, J. Appl. Phys. **84**, 458 (1998).

[18] T. Asada and Y. Koyama, Phys. Rev. B **69**, 104108 (2004).
[19] Y. Cai, F. Phillipp, A. Zimmermann, L. Zhou, F. Aldinger, and M. Rühle, Acta Mater. **51**, 6429 (2003).
[20] See Supplemental Material at http://link.aps.org/supplemental/10.1103/PhysRevLett.123.217602, which includes Refs. [21–27], for experimental details, computational details, a discussion on a bilinear coupling between the Pb displacements and oxygen octahedral tiltings, *P-E* hysteresis loops of bulk samples, HAADF-STEM image simulations, an evaluation of chemistry variation by low-magnification STEM and atomic-scale EDS, and *in situ* electric-biasing TEM results.
[21] F. de la Peña *et al.*, computer code HyperSpy 1.3.2, 2018, http://doi.org/10.5281/zenodo.1304308.
[22] M. Nord, P. E. Vullum, I. MacLaren, T. Tybell, and R. Holmestad, Adv. Struct. Chem. Imaging **3**, 9 (2017).
[23] C. Koch, Ph.D. thesis, Arizona State University, 2002.
[24] P. Lu, L. Zhou, M. J. Kramer, and D. J. Smith, Sci. Rep. **4**, 3945 (2014).
[25] G. Kresse and D. Joubert, Phys. Rev. B **59**, 1758 (1999).
[26] J. P. Perdew, A. Ruzsinszky, G. I. Csonka, O. A. Vydrov, G. E. Scuseria, L. A. Constantin, X. Zhou, and K. Burke, Phys. Rev. Lett. **100**, 136406 (2008).
[27] H. Guo and X. Tan, Phys. Rev. B **91**, 144104 (2015).
[28] Y. Liu, Y. L. Zhu, Y. L. Tang, and X. L. Ma, J. Mater. Res. **32**, 947 (2017).
[29] J. Cui, Y. Yao, Y. G. Wang, X. Shen, and R. C. Yu, Ultramicroscopy **182**, 156 (2017).
[30] W. Zhong, R. D. King-Smith, and D. Vanderbilt, Phys. Rev. Lett. **72**, 3618 (1994).
[31] I. MacLaren, R. Villaurrutia, B. Schaffer, L. Houben, and A. Peláiz-Barranco, Adv. Funct. Mater. **22**, 261 (2012).
[32] K. Patel, S. Prosandeev, Y. Yang, B. Xu, J. Íñiguez, and L. Bellaiche, Phys. Rev. B **94**, 054107 (2016).
[33] B. Xu, O. Hellman, and L. Bellaiche, Phys. Rev. B **100**, 020102(R) (2019).